# MIT Libraries | DSpace@MIT

# MIT Open Access Articles

## *Engineering broadband and anisotropic photoluminescence emission from rare earth doped tellurite thin film photonic crystals*

**Massachusetts Institute of Technology**

# Engineering broadband and anisotropic photoluminescence emission from rare earth doped tellurite thin film photonic crystals

**Pao T. Lin,[1,*] Michiel Vanhoutte,[1,2] Neil S. Patel,[1,2] Vivek Singh,[1,2] Juejun Hu,[3] Yan Cai,[1,2] Rodolfo Camacho-Aguilera,[1,2] Jurgen Michel,[1] Lionel C. Kimerling,[1,2] and Anu Agarwal[1]**

[1]*Microphotonics Center, Massachusetts Institute of Technology, Cambridge, Massachusetts 02139, USA*
[2]*Department of Materials Science and Engineering, Massachusetts Institute of Technology, Cambridge, Massachusetts 02139, USA*
[3]*Department of Materials Science and Engineering, University of Delaware, Newark, Delaware 19716, USA*
*[*]paolin@mit.edu*

**Abstract:** Broadband and anisotropic light emission from rare-earth doped tellurite thin films is demonstrated using $Er^{3+}$-$TeO_2$ photonic crystals (PhCs). By adjusting the PhC parameters, photoluminescent light can be efficiently coupled into vertical surface emission or lateral waveguide propagation modes. Because of the flexibility of light projection direction, $Er^{3+}$-$TeO_2$ is a potential broadband light source for integration with three-dimensional photonic circuits and on-chip biochemical sensors.

## References and links

1. M. Miritello, R. Lo Savio, F. Iacona, G. Franzò, A. Irrera, A. M. Piro, C. Bongiorno, and F. Priolo, "Efficient luminescence and energy transfer in erbium silicate thin films," Adv. Mater. (Deerfield Beach Fla.) **19**(12), 1582–1588 (2007).
2. J. H. Kim and P. H. Holloway, "Near-infrared-electroluminescent light-emitting planar optical sources based on gallium nitride doped with rare earths," Adv. Mater. (Deerfield Beach Fla.) **17**(1), 91–96 (2005).
3. K. Suh, M. Lee, J. S. Chang, H. Lee, N. Park, G. Y. Sung, and J. H. Shin, "Cooperative upconversion and optical gain in ion-beam sputter-deposited $Er_xY_{2-x}SiO_5$," Opt. Express **18**(8), 7724–7731 (2010).
4. M. T. Carlson, A. Khan, and H. H. Richardson, "Local temperature determination of optically excited nanoparticles and nanodots," Nano Lett. **11**(3), 1061–1069 (2011).
5. S. Shen, A. Jha, X. Liu, M. Naftaly, K. Bindra, H. J. Bookey, and A. K. Kar, "Tellurite glasses for broadband amplifiers and integrated optics," J. Am. Ceram. Soc. **85**(6), 1391–1395 (2002).
6. J. S. Wang, E. M. Vogel, and E. Snitzer, "Tellurite glass: a new candidate for fiber devices," Opt. Mater. **3**(3), 187–203 (1994).
7. I. Jlassi, H. Elhouichet, and M. Ferid, "Thermal and optical properties of tellurite glasses doped erbium," J. Mater. Sci. **46**(3), 806–812 (2011).
8. S. Shen, B. Richards, and A. Jha, "Enhancement in pump inversion efficiency at 980 nm in $Er^{3+}$, $Er^{3+}$/$Eu^{3+}$+ and $Er^{3+}$/$Ce^{3+}$ doped tellurite glass fibers," Opt. Express **14**(12), 5050–5054 (2006).
9. M. R. Oermann, H. Ebendorff-Heidepriem, Y. Li, T.-C. Foo, and T. M. Monro, "Index matching between passive and active tellurite glasses for use in microstructured fiber lasers: erbium doped lanthanum-tellurite glass," Opt. Express **17**(18), 15578–15584 (2009).
10. A. Mori, "Tellurite-based fibers and their applications to optical communication networks," J. Ceram. Soc. Jpn. **116**(1358), 1040–1051 (2008).
11. M. Pollnau and S. D. Jackson, "Mid-infrared fiber lasers solid-state mid-infrared laser sources," Top. Appl. Phys. **89**, 219–253 (2003).
12. G. S. Murugan and Y. Ohishi, "$TeO_2$–$BaO$–$SrO$–$Nb_2O_5$ glasses: a new glass system for waveguide devices applications," J. Non-Cryst. Solids **341**(1-3), 86–92 (2004).
13. F. D'Amore, M. Di Giulio, S. M. Pietralunga, A. Zappettini, L. Nasi, V. Rigato, and M. Martinelli, "Sputtered stoichiometric $teo_2$ glass films: dispersion of linear and nonlinear optical properties," J. Appl. Phys. **94**(3), 1654 (2003).
14. N. Dewan, V. Gupta, K. Sreenivas, and R. S. Katiyar, "Growth of amorphous $TeO_x$ ($2 \leq x \leq 3$) thin film by radio frequency sputtering," J. Appl. Phys. **101**(8), 084910 (2007).
15. X. J. Wang, G. Yuan, H. Isshiki, T. Kimura, and Z. J. Zhou, "Photoluminescence enhancement and high gain amplification of $Er_xY_{2-x}SiO_5$ waveguide," Appl. Phys. (Berl.) **108**, 013506 (2010).

16. D. Zhao, S.-J. Seo, and B.-S. Bae, "Full-color mesophase silicate thin film phosphors incorporated with rare earth ions and photosensitizers," Adv. Mater. (Deerfield Beach Fla.) **19**(21), 3473–3479 (2007).
17. M. Boroditsky, T. F. Krauss, R. Coccioli, R. Vrijen, R. Bhat, and E. Yablonovitch, "Light extraction from optically pumped light-emitting diode by thin-slab photonic crystals," Appl. Phys. Lett. **75**(8), 1036 (1999).
18. B. Cluzel, N. Pauc, V. Calvo, T. Charvolin, and E. Hadji, "Nanobox array for silicon-on-insulator luminescence enhancement at room temperature," Appl. Phys. Lett. **88**(13), 133120 (2006).
19. B. Cluzel, V. Calvo, T. Charvolin, E. Picard, P. Noé, and E. Hadji, "Single-mode room-temperature emission with a silicon rod lattice," Appl. Phys. Lett. **89**(20), 201111 (2006).
20. M. Zelsmann, E. Picard, T. Charvolin, E. Hadji, M. Heitzmann, B. Dal'zotto, M. E. Nier, C. Seassal, P. Rojo-Romeo, and X. Letartre, "Seventy-fold enhancement of light extraction from a defectless photonic crystal made on silicon-on-insulator," Appl. Phys. Lett. **83**(13), 2542 (2003).
21. K.-Y. Ko, Y. K. Lee, Y. R. Do, and Y. D. Huh, "Structural effect of a two-dimensional $SiO_2$ photonic crystal layer on extraction efficiency in sputter-deposited $Y_2O_3$:$Eu^{3+}$ thin-film phosphors," J. Appl. Phys. **102**(1), 013509 (2007).
22. K.-Y. Ko, Y. K. Lee, H. K. Park, Y.-C. Kim, and Y. R. Do, "The variation of the enhanced photoluminescence efficiency of $Y_2O_3$:$Eu^{3+}$ films with the thickness to the photonic crystal layer," Opt. Express **16**(8), 5689–5696 (2008).
23. T. Liu and R. Panepucci, "Confined waveguide modes in slot photonic crystal slab," Opt. Express **15**(7), 4304–4309 (2007).
24. C. E. Chryssou, "WDM systems in the C-band using $Er^{3+}$-doped tellurite optical waveguide amplifiers," Fiber Int. Opt. **20**(6), 581–590 (2001).
25. C. E. Chryssou, F. Di Pasquale, and C. W. Pitt, "$Er^{3+}$-doped channel optical waveguide amplifiers for WDM systems: a comparison of tellurite, alumina and Al/P silicate materials," IEEE J. Sel. Top. Quantum Electron. **6**(1), 114–121 (2000).
26. G. N. Conti, S. Berneschi, M. Bettinelli, M. Brenci, B. Chen, S. Pelli, A. Speghini, and G. C. Righini, "Rare-earth doped tungsten tellurite glasses and waveguides: fabrication and characterization," J. Non-Cryst. Solids **345**, 343–348 (2004).
27. K. T. Vu and S. J. Madden, "Reactive ion etching of tellurite and chalcogenide waveguides using hydrogen, methane, and argon," J. Vac. Sci. Technol. A **29**(1), 011023 (2011).
28. R. D. Lide, *CRC Handbook of Chemistry and Physics*, 88th ed. (CRC, 2007).
29. P. Nandi, G. Jose, C. Jayakrishnan, S. Debbarma, K. Chalapathi, K. Alti, A. K. Dharmadhikari, J. A. Dharmadhikari, and D. Mathur, "Femtosecond laser written channel waveguides in tellurite glass," Opt. Express **14**(25), 12145–12150 (2006).
30. S. Sakida, T. Nanba, and Y. Miura, "Refractive-index profiles and propagation losses of $Er^{3+}$-doped tungsten tellurite glass waveguide by $Ag^+$–$Na^+$ Ion-exchange," Mater. Lett. **60**(28), 3413–3415 (2006).
31. S. Sakida, T. Nanba, and Y. Miura, "Optical properties of $Er^{3+}$-doped tungsten tellurite glass waveguides by $Ag^+$–$Na^+$ ion-exchange," Opt. Mater. **30**(4), 586–593 (2007).
32. S. K. Sundaram, C. B. Schaffer, and E. Mazur, "Microexplosions in tellurite glasses," Appl. Phys., A Mater. Sci. Process. **76**(3), 379–384 (2003).
33. Y. Tokuda, M. Saito, M. Takahashi, K. Yamada, W. Watanabe, K. Itoh, and T. Yoko, "Waveguide formation in niobium tellurite glases by pico- and femtosecond laser pulses," J. Non-Cryst. Solids **326–327**, 472–475 (2003).
34. K. Vu and S. Madden, "Tellurium dioxide erbium doped planar rib waveguide amplifiers with net gain and 2.8 dB/cm internal gain," Opt. Express **18**(18), 19192–19200 (2010).
35. S. M. Pietralunga, M. Lanata, M. Ferè, D. Piccinin, G. Cusmai, M. Torregiani, and M. Martinelli, "High-contrast waveguides in sputtered pure $TeO_2$ glass thin films," Opt. Express **16**(26), 21662–21670 (2008).
36. G. N. Conti, V. K. Tikhomirov, M. Bettinelli, S. Berneschi, M. Brenci, B. Chen, S. Pelli, A. Speghini, A. B. Seddon, and G. C. Righini, "Characterization of ion-exchanged waveguides in tungsten tellurite and zinc tellurite $Er^{3+}$-doped glasses," Opt. Eng. **42**(10), 2805 (2003).
37. V. Reboud, N. Kehagias, M. Zelsmann, C. Schuster, M. Fink, F. Reuther, G. Gruetzner, and C. M. Sotomayor Torres, "photoluminescence enhancement in nanoimprinted photonic crystals and coupled surface plasmons," Opt. Express **15**(12), 7190–7195 (2007).
38. A. C. Arsenault, T. J. Clark, G. von Freymann, L. Cademartiri, R. Sapienza, J. Bertolotti, E. Vekris, S. Wong, V. Kitaev, I. Manners, R. Z. Wang, S. John, D. Wiersma, and G. A. Ozin, "From colour fingerprinting to the control of photoluminescence in elastic photonic crystals," Nat. Mater. **5**(3), 179–184 (2006).

## 1. Introduction

Rare earth doped thin films are promising light sources for nanophotonic circuits and biochemical sensors because of their extended emission spectral range and compatibility with monolithic integration [1–4]. Among these active optical glasses, erbium doped $TeO_2$ ($Er^{3+}$-$TeO_2$) thin films have recently attracted a lot of attention because of their extremely high efficiency of photoluminescence (PL) emission. Tellurite glass is known for its high erbium solubility, which significantly increases the concentration of PL emission centers [5,6]. Due to its low maximum phonon energy and high refractive index, $Er^{3+}$-$TeO_2$ exhibits significantly higher emission rate compared to Erbium doped silicates and silicon dioxides [7,8]. Furthermore, tellurite has a broad optical transmission window, which covers a

broadband spectrum from visible to mid-IR up to 4.5 µm. Due to these superior optical properties, $Er^{3+}$-$TeO_2$ based near IR and mid IR fiber lasers and amplifiers have been developed recently [9,10]. To create on-chip light source integrated photonic circuits, tellurite thin films are great candidates because they are compatible with monolithic Si-CMOS processes [11,12]. Furthermore, they can be deposited at room temperature and require no post-annealing [13,14]. For these reasons, $Er^{3+}$-$TeO_2$ thin films are promising broadband light source for chembio-photonic platforms and optical communication systems [15,16].

Despite these promising advantages, introducing flexible angular emission and efficient extraction of broadband PL light remain the most difficult barriers to be overcome in order to achieve an on-chip $Er^{3+}$-$TeO_2$ light source. We already know from studies of light emitting diodes (LEDs) that the efficiency of light extraction determines the performance of thin film light [17]. Previous work by B. Cluzel and M. Zelsmann et al also demonstrated that the PL from silicon-on-insulator can be enhanced by surface patterning [18–20]. Compared to an LED and silicon, an on-chip light source is more difficult because of the need for tunable angular emission and to direct the broadband light into waveguides [21,22]. For in-plane photonic circuits, the PL light must be confined inside the film layer rather than being emitted from the film surface [23–25]. On the other hand, surface PL emission is needed for microfluidic devices, since the fluidic channels are placed beyond or below the $Er^{3+}$-$TeO_2$ layers. Hence, structures that can enhance the anisotropy of PL emission patterns are key to the development of a successful on-chip PL light source.

Besides the challenges in device design for anisotropic PL coupling, difficulties in patterning $Er^{3+}$-$TeO_2$ thin films with submicron resolution also hinder its application as an on-chip light source [26]. Due to the low volatility of tellurite, the use of an etching process for patterning results in undesired columnar structures [27,28]. Other techniques, such as direct laser writing and ion exchange, have been explored [29–31]; however, these are associated with micro-explosion and surface damage, and are accompanied by a degraded pattern resolution [32,33]. Recently, Vu and Madden demonstrated an $Er^{3+}$-$TeO_2$ rib waveguide amplifier: though the amplifier results in a net gain of 2.8 dB /cm, the waveguide has surface roughness in the order of tens of nanometers [34]. The rough surface that is typically produced during etching processes causes significant light loss and prevents its application in nanophotonic devices [35,36]. Collectively, these observations point to the need for alternative fabrication processes that can generate patterns with sub-micron resolution and minimized surface roughness in order to permit use of $Er^{3+}$-$TeO_2$ as an efficient on-chip light source [37].

In this study we have designed and fabricated two dimensional $Er^{3+}$-$TeO_2$ PhCs to accomplish broadband PL emission and enhance its anisotropy. PhCs arrays with different structures are examined to optimize the efficiency of PL extraction [38]. The PhC structures are written by a dual-beam focused ion beam (FIB) which generates patterns with smooth surfaces. Nano-lithography using FIB can easily reach a resolution of hundred nanometers. A confocal microscope with spectrometer is then used to capture the broadband PL signals from individual PhC arrays. The emission enhancement factor and spectral dependent anisotropic extraction are analyzed to uncover the interaction between PL emission and PhC structures. Simulation by calculation of two dimensional finite difference time domain (FDTD) is used to explain the experimentally observed enhancement of PL anisotropy.

## 2. Experimental sections

### 2.1 Erbium-doped tellurite thin film growth

$Er^{3+}$-$TeO_2$ thin films were deposited on a Si wafer by an AJA sputtering system. The sputtering rate was recorded by the quartz crystal thickness monitor. Er targets and $TeO_2$ targets were cosputtered at growth rates of 0.02 nm/s and 1.15 nm/s respectively. The flow rate of Ar was 10 sccm and for $O_2$ was 2 sccm. The power used for sputtering was 80 W for the Er target and 60 W for the $TeO_2$ target. The substrate was maintained at room temperature

during deposition. The deposited film thickness was characterized by profilometer (Veeco Dektak) and a 1µm $Er^{3+}$-$TeO_2$ film was obtained.

## 2.2 Patterning of photonic crystals on $Er^{3+}$-$TeO_2$ thin films

PhCs are patterned on Er-$TeO_2$ thin films by dual beams focused ion beam milling (Zeiss NVision 40). The ion beam current was 1.5 nA and patterning time was 60 s for each PhC array. The patterned photonic lattices range from 300 nm to 1 µm. Each PhC array has an area of 20 µm x 20 µm.

## 2.3 Photoluminescence measurements of $Er^{3+}$-$TeO_2$ thin films

The measurements of the PL spectra and images are performed by Micro-PL mapping system (HORIBA Jobin Yvon). The excitation source is 100 mW 532 nm solid state laser (Laser Quantum). The detector is a single channel indium gallium arsenide (InGaAs) detector with liquid $N_2$ cooling. PL mapping is achieved by scanning the laser in the sample plane, where the sample is moved by a high resolution piezo electric stage. PL spectrum at each point of the sample is collected.

## 3. Results and discussion

### 3.1 Morphology characterization of $Er^{3+}$-$TeO_2$ PhCs

Figure 1 shows the SEM surface image of the patterned $Er^{3+}$-$TeO_2$ PhCs. The insert documents a cross sectional image captured with a tilt angle of 36°. In the SEM images, the black areas are air holes milled by the ion beam, whereas the light gray background is the remaining $Er^{3+}$-$TeO_2$ thin film. The PhC lattice constant **a** is defined by the patterning periodicity, which is 700 nm in Fig. 1. This PhC array has a square symmetry and consists of air columns of 200 nm diameter. Highly smooth vertical edges are observed in the cross sectional image which shows that roughness is minimized through use of ion beam milling. In addition, the milled holes are regularly distributed without any misalignments or distortion. Unlike dry etching or wet etching, no grass effect appears in the milled surface which indicates that the FIB technique is well suited for the fabrication of $Er^{3+}$-$TeO_2$ nanophotonic devices.



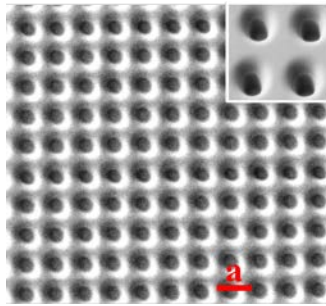Fig. 1. SEM surface image of the patterned $Er^{3+}$-$TeO_2$ thin film PhCs. The insert (upper right) is a cross sectional image captured at a tilt angle of 36°. Photonic lattice constant **a** = 700 nm is labeled by the red bar.

### 3.2 Spectral characterization of the emission from $Er^{3+}$-$TeO_2$ PhCs

Figure 2(a) shows the PL spectrum resulting from excitation of the $Er^{3+}$-$TeO_2$ thin film by a 532 nm laser. A strong PL emission with full width at half maximum (FWHM) of 60 nm is observed between 1475 nm and 1625 nm, with the center wavelength at 1530 nm, which corresponds to the $Er^{3+}$ $^4I_{13/2} \rightarrow {}^4I_{15/2}$ transition. To study the effect of varying PhC structures on PL emission, the spatial profiles of PL signals were recorded. PL mappings at $\lambda = 1500$ nm, 1530 nm and 1560 nm are displayed in Fig. 2(b). Note that $\lambda = 1530$ nm is the center of the PL spectrum, whereas $\lambda = 1500$ nm and $\lambda = 1560$ nm are wavelengths at which the PL

intensities reach half of the maximum. The periodicities of the 2 x 5 PhC array starting from the top right going counterclockwise are 360 nm, 490 nm, 630 nm, 800 nm and 950 nm, 1050 nm, 1180 nm, 1330 nm, 1430 nm, 1670 nm, respectively. The variation of PL signal strength corresponds to the change in intensity of PL surface emission. Higher intensity in the PL mapping indicate that more PL is extracted from the $Er^{3+}$-$TeO_2$ layer into the external medium which is air in this case. In contrast, decreased PL intensity indicates that more PL light is confined inside the $Er^{3+}$-$TeO_2$ layer. The PL that remains in the film is defined as the planar waveguide propagation mode.
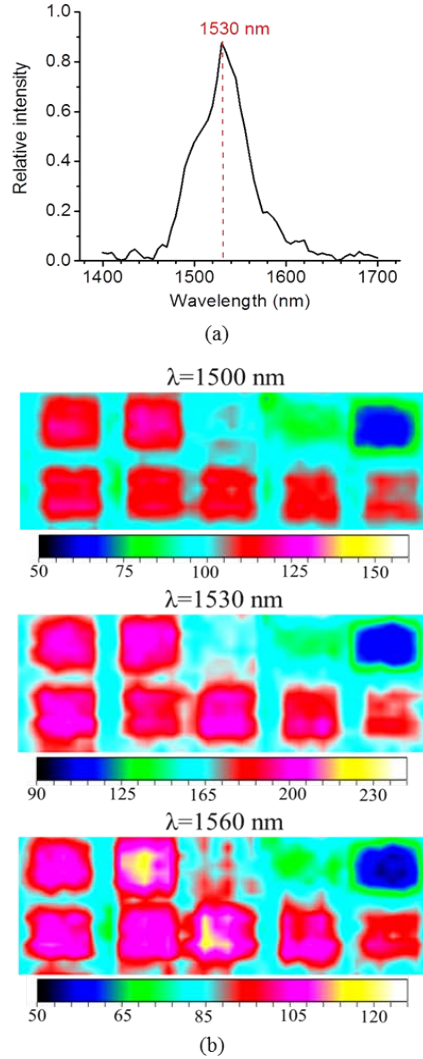


Fig. 2. (a) PL spectrum obtained when the $Er^{3+}$-$TeO_2$ thin film is excited by a 532 nm laser. (b) PL mapping at λ = 1500 nm, 1530 nm and 1560 nm. The periodicities of the 2 x 5 PhC array starting from the top right going counterclockwise are 360 nm, 490 nm, 630 nm, 800 nm and 950 nm, 1050 nm, 1180 nm, 1330 nm, 1430 nm, 1670 nm, respectively. Below the PL mapping is the scale bar at different λ.

To better interpret this variation in PL, we used $F_S$, the enhancement factor for surface PL emission, to analyze the dependence of PL intensity on the PhC periodicity **a**. $F_S$ is defined as follows:

$$F_s = \frac{I_s - I_{sb}}{I_{sb}}$$

where $I_s$ is the PL intensity measured at the surface of the PhCs, and $I_{sb}$ is the surface intensity from the non-patterned area. A plot of $F_S$ at different **a** and λ is shown in Fig. 3. At PL spectrum center, λ = 1530 nm, destructive surface PL is observed at **a** = 360 nm, while a strongly enhanced surface PL is observed between **a** = 800 nm and **a** = 1330 nm. Plots of $F_S$ vs. **a** reveal that, for all PL wavelengths, $F_S$ factors are negative when **a** is smaller than 600 nm, indicating that PhCs with **a** = 360 nm can efficiently direct the broadband PL light into waveguide propagation mode. On the other hand, PhCs with **a** = 800 nm, **a** = 950 nm, and **a** = 1050 nm have significantly high $F_S > 40\%$ in the entire PL spectral range. Hence, PhCs from **a** = 800 nm to **a** = 1050 nm can project most PL light into the air. As shown in Fig. 3, $F_S$ remains positive in the entire PL spectrum when periodicity **a** is larger than 600 nm which indicates that surface emission is the preferential mode when the PL light interacts with wider photonic lattices. Therefore the PL mapping results and the plots of $F_S$ vs. **a** demonstrate that by tuning the periodicity **a,** we can readily select the desired PL emission modes which also determine the PL projection directions. Depending on the layout of the integrated system, $Er^{3+}$-$TeO_2$ PhCs can supply broadband light into in-plane optical circuits such as waveguides, as well as out-of-plane sensors such as monolithic detectors or microfluidic channels. The flexibility of vertical and in-plane emission enables the design of three dimensional photonic circuits. Hence, these $Er^{3+}$-$TeO_2$ PhCs arrays can potentially serve as broadband on-chip light sources with adjustable emission directions.
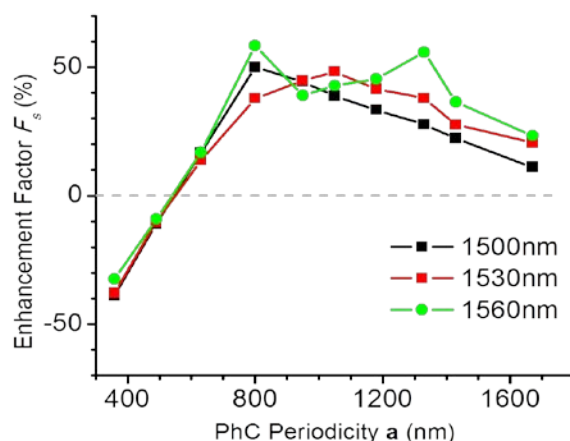


Fig. 3. PL surface enhancement factor $F_S$ measured at different PhC periodicities **a** and PL wavelengths λ.

From Fig. 3 we see that PL at shorter wavelength, λ = 1500 nm, has a similar mapping result to PL at λ = 1530 nm. We determine that the PL intensity in the absence of PhCs is 90 counts at λ = 1500 nm. For PhCs with the smallest periodicity, **a** = 360 nm, a strongly destructive surface PL of 55 counts is observed, while a slightly destructive PL of 80 counts appears at **a** = 490 nm. When **a** = 630 nm, no effect on PL is found. As **a** increases to 800 nm, a highly enhanced surface PL of 135 counts is obtained; this highly bright surface PL continues at **a** = 950 nm and **a** = 1050 nm. Though the surface PL remains enhanced from **a** = 1180 to **a** = 1670 nm, its intensity gradually decreases from 120 accounts to 100 accounts. From Fig. 3, $F_S$ increases from −39% at **a** = 360 nm to 50% at **a** = 800 nm. We note also that the waveguide propagation mode is preferred when $F_S$ is negative. Hence, PL remains inside the thin film layer at **a** = 360 nm. As **a** increases, PL emission is redirected from in-plane to out-of-plane, which indicates a mode transition from waveguide propagation to surface emission. At **a** = 800 nm, the PL extraction ratio is increased by 50% and has reached its maximum. As **a** increases beyond 800 nm, $F_S$ gradually decreases indicating that the PL light

becomes more evenly distributed between surface emission and waveguide propagation. The plot of $F_S$ vs. **a** shows that PhCs have less effect on PL emission when periodicity **a** is > 1600 nm.

We also investigated the broadband properties of surface PL enhancement by mapping PL intensities at longer wavelengths, $\lambda$ = 1560 nm, as shown in Fig. 2(b). The relationship between the enhancement factor $F_S$ and the PhC periodicity **a** is plotted in Fig. 3. Though the preferential mode is independent of the wavelength of the PL, the response of the enhancement factor $F_S$, varies as the wavelengths of the PL shift when periodicity **a** increases. At $\lambda$ = 1500 nm, $F_S$ reaches its maximum at **a** = 800 nm; then as **a** increases from 800 nm to 1670 nm, $F_S$ linearly decreases from 50% to 11%. As the wavelength of PL shifts to $\lambda$ = 1530 nm, the periodicity of maximum $F_S$ moves to **a** = 1180 nm, after which $F_S$ monotonically decreases from 48% to 21% at **a** = 1670 nm. In other words, a 30 nm red shift of $\lambda$ causes a shift in the optimized periodicity from **a** = 800 nm to **a** = 1180 nm, is significant change of **a** by 380 nm. Unlike the plots of $F_S$ vs. **a** at $\lambda$ = 1500 nm and $\lambda$ = 1530 nm, where only a single optimized **a** exists, the optimized periodicity degenerates to **a** = 800 nm and **a** = 1330 nm when $\lambda$ = 1560 nm. The two maximum $F_S$ at $\lambda$ = 1560 nm are 58% and 56%, which are 10% higher than the maximum $F_S$ obtained at shorter PL wavelengths. The plot of $F_S$ vs. **a** also shows that PhCs which have periodicities **a** = 800 nm, **a** = 950 nm, and **a** = 1050 nm are the optimal structures for broadband PL surface emission. Though a PhC with **a** = 1333 nm has an extremely high $F_S$ factor at $\lambda$ = 1560 nm, its relatively low $F_S$ at shorter PL wavelengths prohibits its application for broadband PL surface coupling.

In a similar vein, PhCs with periodicities **a** that are smaller than 600 nm have very consistent response along the entire PL spectrum. Figure 3 documents that PhCs with **a** = 360 nm have $F_S$ factors of – 40% at all PL wavelengths. Therefore, such a PhC can well confine the broadband PL light within the $Er^{3+}$-$TeO_2$ layer without any light leaking into the external media. For applications of integrated circuits, such PhCs can be used as a broadband on-chip coupler, which redirects the PL light into nearby optical waveguides or micro-resonators.

*3.3 FDTD simulation of the emission intensities of $Er^{3+}$-$TeO_2$ PhCs and the propagation modes*

Two dimensional FDTD simulations were performed to investigate the switching mechanism between the PL surface emission mode and waveguide propagation mode. The structure in the calculation is shown in Fig. 4 and the follwoing is the detailed simulation conditions: The middle layer (From y = 0 to y = 1) is a 1 µm PhC $Er^{3+}$-$TeO_2$ layer, with a refractive index of 2.3. The botton layer is the Si and the top layer is air. The PhC array is composed of twenty photonic crytsal lattices with periodicities **a**. A broadband dipole source from $\lambda$ = 1.45 µm to 1.65 µm is placed in the center photonic lattice at x = 0 and y = 0.5. One sensor box is placed around the PhC array in order to calculate the fluxes propagating through the top, bottom, left and right interfaces. Perfectly matched layer is used as the boundary condition. In order to achieve highly accurate modeling, the size of the calculation step is chosen to be 20 nm. The duration of simulation is set to 5000 fs to ensure that light can pass through the sensor even when resonance occurs inside the PhCs.
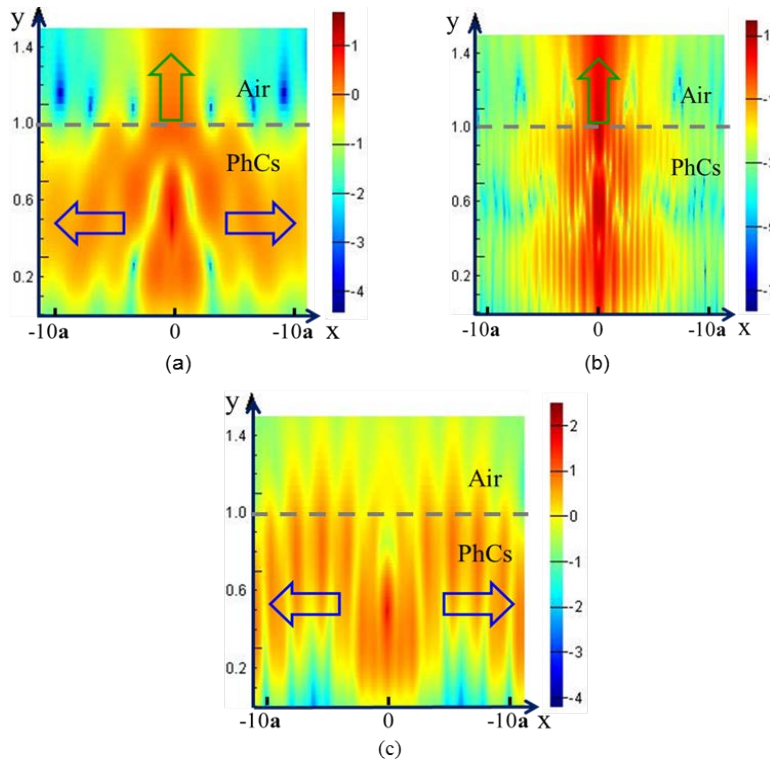
Fig. 4. The simulated patterns of PL emission at λ = 1530 nm (a) without PhC structure, (b) with **a** = 800 nm PhC array, and (c) with **a** = 300 nm PhC array. The film thickness is 1 um (From y = 0 to y = 1). The green arrows and the blue arrows indicate the surface emission and the waveguide propagation, respectively.

The PL emission patterns for different structures at λ = 1530 nm are displayed in Figs. 4(a)–4(c). Figure 4(a) shows the PL intensity profile of a film when there is no PhC array. The PL light from the center dipole is uniformly emitted in horizontal and vertical directions, and the PL fluxes passing through the top sensor and the side sensor are of the same order of magnitude. For the surface emission, a small cone of PL radiation is observed, whereas for the side emission, the PL propagates laterally inside the $Er^{3+}$-$TeO_2$ layer and the light wave bounces back and forth between two interfaces: air to $Er^{3+}$-$TeO_2$ film and $Er^{3+}$-$TeO_2$ film to Si wafer. For comparison, the PL intensity profile from a PhC array at **a** = 800 nm is shown in Fig. 4(b). A strong PL signal is observed at the top film surface where the PL light is projected upward to the air. Clearly, the PhC induces a highly anisotropic emission pattern; the surface PL is almost four orders of magnitude higher than lateral PL. The PL profile illustrates that the PhC array significantly enhances the extraction of the surface PL. On the other hand, Fig. 4(c) shows that the PhC with **a** = 300 nm has a highly confined waveguide mode; the PL intensity detected from the side sensor is four times higher than the intensity read by the top sensor. This indicates that most PL light remains in the $Er^{3+}$-$TeO_2$ film layer since surface PL extraction is strongly suppressed. As PhC periodicities decrease from **a** = 800 nm to **a** = 300 nm, the side PL signal is enhanced by four orders of magnitude. Figures 4(a)–4(c) document that the PL emission patterns from $Er^{3+}$-$TeO_2$ thin films can be readily manipulated by optimizing the structure of the PhCs, and switching between the surface emission mode and waveguide propagation mode is achieved by adjusting the PhC periodicity **a**.

Enhancement factors *F* at different PhC periodicities **a** are calculated and drawn in Fig. 5 in order to investigate the dependence of anisotropic PL emission on the PhC structures. In

the equations below, $F_S$ and $F_W$ are the PL enhancement factors for the surface emission mode and the waveguide propagation mode respectively. They are defined as follows:

$$F_s = \frac{I_s - I_{sb}}{I_{sb}}$$

$$F_w = \frac{I_w - I_{wb}}{I_{wb}}$$

$I_s$ is the PL intensity above the air – $Er^{3+}$-$TeO_2$ interface, where the light is extracted from the emission layer; $I_w$ is the lateral PL signal observed at the edges of the $Er^{3+}$-$TeO_2$ film and refers to the PL in the waveguide planar mode. Both $I_s$ and $I_w$ are measured in the presence of a PhC array. $I_{sb}$ and $I_{wb}$ are the backgrounds PL signals for the two modes when no PhC structure exists. We find that surface PL enhancement factors $F_S$ are positive when periodicity **a** is larger than 500 nm. A maximum $F_S$ is observed for PhC with **a** = 800 nm while the waveguide PL enhancement factor $F_W$ is negative when **a** is larger than 400 nm. Together the positive $F_S$ and negative $F_W$ indicate that surface emission is dominant, and the PL waveguide confinement is depressed. Therefore, the PhCs structure can efficiently extract PL light from $Er^{3+}$-$TeO_2$ layers into the air. In contrast, $F_S$ becomes negative when **a**<500 nm while $F_W$ becomes positive, and sharply increases from −50% to + 50% when **a** approaches 350 nm. The change of both factors, $F_W$ (negative to positive) and $F_S$ (positive to negative), reveals that most PL light is confined inside the $Er^{3+}$-$TeO_2$ layer appears in a waveguide propagation mode.
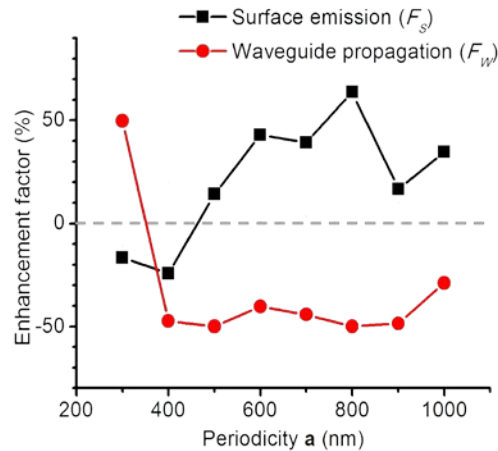


Fig. 5. Enhancement factors $F_S$ and $F_W$ simulated at different PhC periodicities **a**.

Note that the plot of $F$ vs. **a** drawn from results of the simulation shows the same tendency as for the $F$ vs. **a** plot shown in Fig. 3 (derived from experimental data). Both plots reveal that the critical PhC periodicity $a_C$ triggers a mode transition. When **a** > $a_C$, surface PL emission is preferred, and as the value of **a** decreases, $F_S$ also gradually decreases while $F_W$ remains negative. Once **a** reaches $a_C$, $F_S$ turns negative and $F_W$ increases rapidly. This explains why the PL mapping shown in Fig. 2(b) exhibits destructive surface PL at **a** = 360 nm. Another tendency seen in the $F$ vs. **a** plot is the existence of maximum $F_S$. Instead of monotonically increasing with the periodicity **a**, $F_S$ reaches its highest value, 1.3, at **a** = 800 nm then decreases. These results correspond to the plot of measured $F_S$ vs. **a** in Fig. 3 in which the maximum $F_S$ value is observed between **a** = 800 nm and **a** = 1100 nm. Hence, the $F$ vs. **a** relationship derived from FDTD simulation agrees well with the $F_S$ vs. **a** variation observed experimentally. This varies that the anisotropic PL emission from $Er^{3+}$-$TeO_2$ PhCs can be accurately predicted by the simulation. Also, by modulating the percentage of PhC structures we can easily enhance the PL extraction ratio and determine the PL projection patterns.

To explain the anisotropic emission, the photonic band structure of $Er^{3+}$-$TeO_2$ PhCs is calculated and shown in Fig. 6. From the diagram we find two photonic band gaps. The first gap is from 0.25f to 0.3f, where f is the normalized frequency equal to $\mathbf{a}$/c Hz. The second gap is from 0.48f to 0.55f with a narrow band in the gap center. For a PhC with periodicity $\mathbf{a}$ = 800 nm, the second gap covers from $\lambda$ = 1455 nm to 1667 nm. Clearly this band gap overlaps with the PL emission spectrum of $Er^{3+}$-$TeO_2$, and it prohibits the in-plane light propagation of emitted PL. Under this circumstance, only the surface emission mode exists and the enhancement factor of surface extraction $F_S$ reaches its maximum at $\mathbf{a}$ = 800 as shown in Fig. 5. On the other hand, for PhCs at $\mathbf{a}$ = 300 nm PL at wavelength $\lambda$ = 1530 nm has a normalized frequency f = 0.2. Since there is no band gap below f = 0.25, the PL light can easily couple into the thin film layer as the waveguide propagation mode. It explains the rapid increase of $F_W$ when the periodicity $\mathbf{a}$ approaches 300 nm as shown in Fig. 5. Hence, the calculated band structure interprets the observed anisotropic patterns from PL emission and the transition of modes between the surface extraction and waveguide propagation.
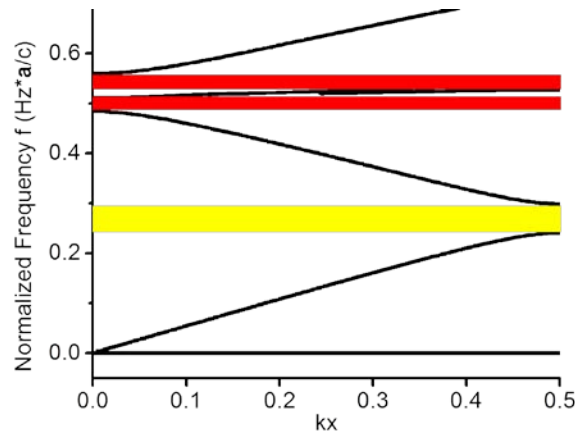


Fig. 6. Calculated photonic band diagram of $Er^{3+}$-$TeO_2$ PhCs. The yellow and red bars indicate the 1st and the 2nd photonic band gaps, respectively. kx is the wavevector in the $\Gamma$-X direction.

To investigate the broadband properties of PL enhancement, anisotropic emission enhancement factors $F_S$ and $F_W$ from $\lambda$ = 1.50 µm to $\lambda$ = 1.56 µm were analyzed. The PL intensities in the surface extraction mode and waveguide propagation modes were calculated by 2-D FDTD simulation. Figure 7(a) shows the spectral $F_S$ and $F_W$ values for PhCs with $\mathbf{a}$ = 800 nm. This value for $\mathbf{a}$ was chosen based on findings shown in Fig. 5 where a PhC with $\mathbf{a}$ = 800 nm had the highest surface emission ratio). As shown in Fig. 7(a), $F_S$ is 80% at $\Delta$ = 1.50 µm, and it drops to 55% at $\Delta$ = 1.56 µm. Therefore, though $F_S$ decreases as the wavelength of the PL increases, enhancement of surface emission beyond 50% is observed over the entire PL spectrum. Meanwhile $F_W$ remains −50% over the entire PL spectrum implying that the planar waveguide mode PL has been suppressed. Therefore, we have demonstrated that the PhC with $\mathbf{a}$ = 800 nm can significantly improve the efficiency of broadband surface extraction.
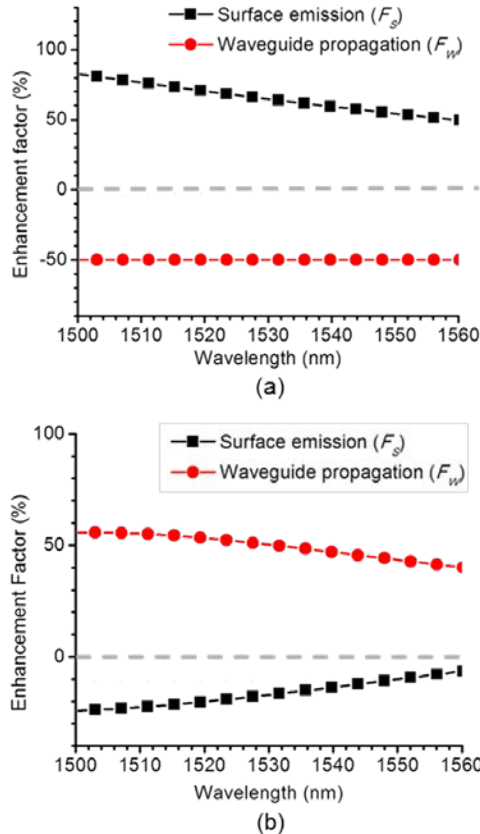
Fig. 7. Anisotropic emission enhancement factors $F_S$ and $F_W$ from $\lambda = 1.50$ µm to $\lambda = 1.56$ µm for PhCs with (a) **a** = 800 nm and (b) **a** = 300 nm.

Spectral enhancement factors for a PhC with **a** = 300 nm are also characterized and shown in Fig. 7(b) since this PhC demonstrates a strong waveguide propagation mode. The enhancement factor for the waveguide mode $F_W$ is 55% at $\lambda = 1.50$ µm and slightly decreases to 45% at $\lambda = 1.56$ µm while surface emission enhancement $F_S$ increases from $-25\%$ to $-10\%$ with an increase in PL wavelength. An averaged $F_W$ of 50% is demonstrated in the overall PL spectra. By using PhCs with **a** = 300 nm, the broadband PL can be highly confined in the $Er^{3+}$-$TeO_2$ layer. Figure 7(a) and 7(b) thus document that the emission pattern can be spatially modulated according to the needs of the integrated photonic devices. PL enhancement exhibits a low variation as the emission wavelength changes. Broadband PL emission can be anisotropically projected into in-plane micro-cavities or adjacent layers with biochemical sensors.

## 4. Conclusion

In conclusion, we have demonstrated that $Er^{3+}$-$TeO_2$ thin films using PhC structures can serve as a broadband nano-optical coupler between two emission modes: the surface PL mission and waveguide PL propagation. By optimizing the PhC structure, 1500 nm-1560 nm broadband PL emission from $Er^{3+}$-$TeO_2$ is successfully converted between these anisotropic modes. 60% enhancement of surface extraction efficiency is achieved when PhC with periodicity **a** = 800 nm is applied. 85% enhancement is observed for waveguide PL emission, at **a** = 300 nm. The high level of flexibility of emission mode selection and the enhancement of broadband PL make $Er^{3+}$-$TeO_2$ PhCs thin films a potential light source for three dimensional integrated photonic circuits.

**Acknowledgments**